Journal of Computational Physics 287 (2015) 207–225

Contents lists available at ScienceDirect

Journal of Computational Physics

www.elsevier.com/locate/jcp

Generalized coordinate transformation and gas-kinetic scheme

Liang Pan, Kun Xu *

Department of Mathematics, Hong Kong University of Science and Technology, Clear Water Bay, Kowloon, Hong Kong

ARTICLE INFO

Article history:
Received 3 March 2014
Received in revised form 25 November 2014
Accepted 3 February 2015
Available online 11 February 2015

Keywords:
Generalized coordinate transformation
Moving-mesh method
Gas-kinetic scheme

ABSTRACT

Under a generalized coordinate transformation with inclusion of both mesh velocity and acceleration, the gas-kinetic equation is transformed from a physical space to a computational space. With the WENO reconstruction, a high-order moving-mesh multidimensional gas-kinetic method, with inclusion of both normal and tangential derivatives of macroscopic flow variables, is constructed. High-order accurate Navier–Stokes solutions are obtained in the current scheme by integrating the numerical fluxes along a cell interface and over a whole time step, without using the conventional Gaussian point integration for spatial accuracy and Runge–Kutta method for temporal accuracy. For the first time, the mesh acceleration has been explicitly accounted for in the flux evaluation. Under the generalized coordinate transformation, a three-dimensional moving-mesh gas-kinetic scheme has been constructed as well. The importance of multi-dimensionality in the flux evaluation and mesh movement is illustrated through numerical tests.

© 2015 Elsevier Inc. All rights reserved.

1. Introduction

In computational fluid dynamics, there exist two coordinate systems to describe flow motions [20]. One is the Eulerian system which describes flow motions with time-independent mesh; the other one is the Lagrangian one, where the mesh moves with the fluid velocity. Based on the above two descriptions, many numerical methods have been developed. Mathematically, these two coordinate systems are proved to be equivalent only in one dimensional case, but are mathematically different in multidimensional ones. Numerically, the schemes based on these two coordinate system are fully different in all dimensions [12,2,8,28,32,33]. Both descriptions have advantages and drawbacks. Generally, the Eulerian system is relatively simple, but it smears contact discontinuities and slip lines badly. On the other hand, the Lagrangian system could resolve contact discontinuities sharply, but computation can easily break down due to mesh deformation. For the computation with fixed boundaries, the Eulerian system could work effectively. However, in the problems with moving boundaries and bodies, it becomes difficult for the Eulerian method. It becomes favorable to develop moving mesh methods for a deforming domain [29]. Currently, there are many moving-mesh methods in literature. One example is the static mesh movement method, where a new mesh is generated at each moment according to a pre-defined monitor function and flow variables are re-distributed to the new mesh [31,30]. Another one is the dynamical moving-mesh method, in which the mesh moves according to mesh velocity, and flow variables are updated automatically inside each time-dependent control volume.

In recent years, a moving-mesh method based on unified coordinate transformation has been developed [11–13]. Under such a transformation with a prescribed mesh velocity, fluid dynamic equations can be transformed from a physical space (t, x, y) to a computational space (σ, ξ, η), with the inclusion of geometric conservation law to record the mesh deforma-

* Corresponding author.
E-mail addresses: panliangjlu@sina.com (L. Pan), makxu@ust.hk (K. Xu).

http://dx.doi.org/10.1016/j.jcp.2015.02.010
0021-9991/© 2015 Elsevier Inc. All rights reserved.

tion. As a result, the fluid dynamic equations and geometric evolution equations are coupled in an enlarged system. And the flow and geometrical variables can be updated simultaneously. In order to avoid disadvantages of excessive numerical diffusion in the Eulerian method and of severe grid deformation in the Lagrangian methods, a dynamical adaptive mesh velocity can be used, and the Eulerian and Lagrangian methods become the limiting cases of the unified scheme. For viscous flow simulations, the Navier–Stokes equations become extremely complicated under the unified coordinate transformation [17]. Among all previous approaches, a constant mesh velocity within each time step is numerically adopted. In aerodynamic applications, for the accurate capturing of aerodynamic movement besides the mesh velocity, the inclusion of a mesh acceleration may be helpful. For example, for an oscillating airfoil, there is definitely acceleration within each time step if the mesh is attached to the surface of the airfoil. Therefore, the development of the moving mesh method with both mesh velocity and acceleration deserves investigation.

The gas-kinetic scheme (GKS) based on the Bhatnagar–Gross–Krook (BGK) model [3–5] has been developed systematically for the compressible flow computations [34,36,14,19,16,38,25]. The gas-kinetic scheme presents a gas evolution process from a kinetic scale to a hydrodynamic scale, where both inviscid and viscous fluxes are recovered from moments of a single time-dependent gas distribution function. In discontinuous shock region, the kinetic scale physics, such as particle free transport through upwinding, takes effect to construct a crisp and stable shock transition due to its inclusion of highly non-equilibrium mechanism in the time-dependent flux function. In smooth flow region, the hydrodynamic scale physics corresponding to the multi-dimensional central difference discretization will contribute mainly in the kinetic flux function, and accurate Navier–Stokes solution can be obtained once the flow structure is well resolved. With discretization of particle velocity space, a unified gas-kinetic scheme (UGKS) has been developed recently for the flow study in entire Knudsen number regimes from rarefied to continuum ones [37,26]. Recently, with incorporation of high-order initial reconstruction, high-order gas-kinetic schemes for the Navier–Stokes equations have been constructed [22,27]. The flux evaluation in the scheme is based on a time evolution of flow variables from an initial piece-wise discontinuous polynomials around a cell interface, where high-order spatial and temporal derivatives of a gas distribution function are coupled nonlinearly. Based on the unified coordinate transformation [11], a moving-mesh gas-kinetic scheme has been developed in [17]. Under such a transformation, the gas-kinetic equation and geometrical conservation laws are combined in an enlarged system. Same as Hui's methods [11,12], both physical and geometrical variables are updated simultaneously. Due to its kinetic nature, the scheme presents the Navier–Stokes solutions directly without referring to the complicated Navier–Stokes equations under the unified coordinate transformation.

In this paper, for the first time, a generalized coordinate transformation with inclusion of both mesh velocity and mesh acceleration will be introduced. With such a coordinate transformation, the gas-kinetic equation will be transformed from a physical space to a computational one. The unified coordinate [11,17] transformation without mesh acceleration becomes a subset of the current one. With the WENO technique for the initial data reconstruction, a high-order moving mesh gas-kinetic scheme will be developed for a deforming control volume with a moving and accelerating cell interface. The numerical fluxes are obtained by taking moments of a time-dependent gas distribution function. A few choices have been used in the determination of mesh velocity. This scheme is applied to both inviscid and viscous flow computations. Under the generalized coordinate transformation, a three-dimensional scheme has been developed as well.

This paper is organized as follows. Section 2 introduces the generalized coordinate transformation. Based on such a transformation, the corresponding kinetic equation in the computational domain is constructed. Section 3 presents the detailed formulation of the scheme with both mesh velocity and acceleration. Section 4 includes numerical examples to validate the current scheme. The last section is the conclusion.

2. Generalized coordinate transformation

With consideration of both mesh velocity (U_g, V_g) and acceleration (a, b), a generalized coordinate transformation from a physical domain (t, x, y, u, v) to a computational domain $(\sigma, \xi, \eta, u', v')$ can be expressed as

$$\begin{aligned} dt &= d\sigma \\ dx &= U_g d\sigma + A d\xi + L d\eta \\ dy &= V_g d\sigma + B d\xi + M d\eta \\ du &= a d\sigma + A du' + L dv' \\ dv &= b d\sigma + B du' + M dv', \end{aligned} \tag{1}$$

where the geometric variables (A, B, L, M) are defined as

$$A = \frac{\partial x}{\partial \xi},\ B = \frac{\partial y}{\partial \xi},\ L = \frac{\partial x}{\partial \eta},\ M = \frac{\partial y}{\partial \eta}. \tag{2}$$

This transformation will go back to the unified coordinate transformation when the last two equations related to the mesh acceleration are absent [11,12]. The inverse of this transformation can be written as

$$\frac{\partial(\sigma,\xi,\eta,u',v')}{\partial(t,x,y,u,v)}=\frac{1}{\Delta^2}\begin{pmatrix}\Delta^2 & 0 & 0 & 0 & 0\\ -I_g\Delta & M\Delta & -L\Delta & 0 & 0\\ -J_g\Delta & -B\Delta & A\Delta & 0 & 0\\ -\alpha\Delta & 0 & 0 & M\Delta & -L\Delta\\ -\beta\Delta & 0 & 0 & -B\Delta & A\Delta\end{pmatrix}, \tag{3}$$

where $\Delta = AM - BL$, $I_g = MU_g - LV_g$, $J_g = AV_g - BU_g$, $\alpha = Ma - Lb$, and $\beta = Ab - Ba$. Theoretically, based on the above transformation, we can transfer the Euler and Navier–Stokes equations from the physical space to the computational space. And their formulations will become extremely complicated. Since we are going to develop a moving-mesh gas-kinetic scheme, the above coordinate transformation will be used to the gas-kinetic BGK equation.

The BGK model in two-dimensional case can be written as

$$f_t + uf_x + vf_y = \frac{g-f}{\tau}, \tag{4}$$

where f is the gas distribution function, g is the corresponding equilibrium state, and τ is the collision time. The collision term satisfies the compatibility condition

$$\int \frac{g-f}{\tau}\psi d\Xi = 0, \tag{5}$$

where $\psi = (1, u, v, \frac{1}{2}(u^2+v^2+\varsigma^2))$, $d\Xi = dudvd\varsigma^1\ldots d\varsigma^K$, K is the number of internal degree of freedom, i.e., $K = (4-2\gamma)/(\gamma-1)$ for two-dimensional flows, and γ is the specific heat ratio. With the inverse transformation (3), on a moving interface, Eq. (4) can be rewritten as

$$\begin{aligned}\frac{\partial}{\partial\sigma}(\Delta f) + \frac{\partial}{\partial\xi}([(u-U_g)M-(v-V_g)L]f) + \frac{\partial}{\partial\eta}([-(u-U_g)B+(v-V_g)A]f)\\ -(Ma-Lb)\frac{\partial f}{\partial u'} - (Ab-Ba)\frac{\partial f}{\partial v'} = \frac{g-f}{\tau}\Delta.\end{aligned} \tag{6}$$

Based on the above transformed BGK equation, both the Euler and the Navier–Stokes equations can be derived using the Chapman–Enskog expansion in the moving space, and the formulations will be much more complicated than these without mesh acceleration [17]. Fortunately, the numerical scheme for the flow simulation in this paper will be based on the kinetic formulation, where the explicit forms of macroscopic equations are not needed.

With both the mesh velocity and acceleration in a physical space, the finite volume scheme in the computational space becomes

$$\begin{aligned}Q_{ij}^{n+1} = Q_{ij}^n &+ \frac{1}{\Delta\xi\Delta\eta}\int_{\sigma^n}^{\sigma^{n+1}}\int_{-\frac{\Delta\eta}{2}}^{\frac{\Delta\eta}{2}}(F_{i-\frac{1}{2},j}(\sigma,\eta)-F_{i+\frac{1}{2},j}(\sigma,\eta))d\eta d\sigma\\ &+ \frac{1}{\Delta\xi\Delta\eta}\int_{\sigma^n}^{\sigma^{n+1}}\int_{-\frac{\Delta\xi}{2}}^{\frac{\Delta\xi}{2}}(G_{i,j-\frac{1}{2}}(\sigma,\xi)-G_{i,j+\frac{1}{2}}(\sigma,\xi))d\xi d\sigma,\end{aligned} \tag{7}$$

where $Q = (\Delta\rho, \Delta\rho U, \Delta\rho V, \Delta\rho E)$ are the flow variables with a time-dependent control volume Δ, $F_{i+1/2,j}$ and $G_{i,j+1/2}$ are corresponding fluxes at ξ and η directions. To update the flow variables, the numerical fluxes need to be evaluated.

3. Moving-mesh gas-kinetic scheme

3.1. Gas-kinetic scheme with mesh velocity only

Without mesh acceleration, the kinetic equation under unified coordinate transformation (1) reduces to the original one in [17,12], Eq. (6) can be simplified as

$$\frac{\partial}{\partial\sigma}(\Delta f) + \frac{\partial}{\partial\xi}([(u-U_g)M-(v-V_g)L]f) + \frac{\partial}{\partial\eta}([-(u-U_g)B+(v-V_g)A]f) = \frac{g-f}{\tau}\Delta. \tag{8}$$

The related scheme in [17] is summarized in the following.

To construct the numerical fluxes $F_{i+1/2,j}$ at the interface $\xi_{i+1/2} = \text{constant}$, Eq. (8) can be further simplified. At a cell interface, the normal and tangential directions are defined as

$$\mathbf{n} = \nabla\xi/\|\nabla\xi\| = (M,-L)/S,$$

$$\mathbf{t} = (L,M)/S,$$

where $S=\sqrt{M^2+L^2}$ is the length of cell interface. The relative velocity projected on the normal direction $\mathbf{n}$ and tangential direction $\mathbf{t}$ can be written as

$$\begin{cases}\widetilde{u}=(u-U_g)M/S-(v-V_g)L/S,\\ \widetilde{v}=(u-U_g)L/S+(v-V_g)M/S.\end{cases} \tag{9}$$

With these notations, the BGK model (8) can be transformed to

$$\frac{\partial f}{\partial\sigma}+\frac{\partial(\widetilde{u}f)}{\partial\widetilde{\xi}}+\frac{\partial(\widetilde{v}f)}{\partial\widetilde{\eta}}=\frac{g-f}{\tau}, \tag{10}$$

where $\widetilde{\xi}$ and $\widetilde{\eta}$ are the distances from a cell interface center in the physical space in the normal and tangential directions. For simplicity, in the following part, σ, $\widetilde{\xi}$ and $\widetilde{\eta}$ will be denoted as t, ξ and η. In a local moving frame of reference, the equilibrium state can be defined by

$$g=\rho(\frac{\lambda}{\pi})^{\frac{K+2}{2}}e^{-\lambda[(\widetilde{u}-\widetilde{U})^2+(\widetilde{v}-\widetilde{V})^2+\varsigma^2]},$$

where $(\widetilde{U},\widetilde{V})$ are the macroscopic relative velocities defined as

$$\widetilde{U}=[(U-U_g)M-(V-V_g)L]/S,$$
$$\widetilde{V}=[(U-U_g)L+(V-V_g)M]/S,$$

and $\lambda=\rho/2p$.

Once the gas distribution function on a moving cell interface is obtained, which will be presented in the next section, the numerical fluxes could be obtained by taking moments of the distribution function

$$\begin{pmatrix}F_{\widetilde{\rho}}\\ F_{\widetilde{\rho u}}\\ F_{\widetilde{\rho v}}\\ F_{\widetilde{E}}\end{pmatrix}_{i+1/2,j}=\int\widetilde{u}\begin{pmatrix}1\\ \widetilde{u}\\ \widetilde{v}\\ \frac{1}{2}(\widetilde{u}^2+\widetilde{v}^2+\varsigma^2)\end{pmatrix}f(\xi_{i+1/2},t,\widetilde{u},\widetilde{v},\varsigma)d\widetilde{u}d\widetilde{v}d\varsigma. \tag{11}$$

In order to update the flow variables inside each time-dependent computational cell, the conservative variables need be to updated relative to a common inertia frame of reference. Therefore, we need to transfer the above fluxes which are evaluated standing on a moving cell interface (11) to the fluxes in the inertia frame of reference. These transformed time-dependent numerical fluxes are given by

$$F_{i+1/2,j}=\begin{pmatrix}F_\rho\\ F_m\\ F_n\\ F_E\end{pmatrix}_{i+1/2,j}=\int S\widetilde{u}\begin{pmatrix}1\\ u\\ v\\ \frac{1}{2}(u^2+v^2+\varsigma^2)\end{pmatrix}f(\xi_{i+1/2},t,\widetilde{u},\widetilde{v},\varsigma)d\widetilde{u}d\widetilde{v}d\varsigma. \tag{12}$$

According to Eq. (9), the above fluxes $F_{i+1/2,j}=(F_\rho,F_m,F_n,F_E)$ on the inertia frame of reference can be obtained as a combination of the fluxes in the moving frame of reference,

$$\begin{cases}F_\rho=SF_{\widetilde{\rho}},\\ F_m=SU_gF_{\widetilde{\rho}}+(MF_{\widetilde{\rho u}}+LF_{\widetilde{\rho v}}),\\ F_n=SV_gF_{\widetilde{\rho}}+(-LF_{\widetilde{\rho u}}+MF_{\widetilde{\rho v}}),\\ F_E=SF_{\widetilde{E}}+(MU_g-LV_g)F_{\widetilde{\rho u}}+(LU_g+MV_g)F_{\widetilde{\rho v}}+\dfrac{S}{2}[(U_g^2+V_g^2)F_{\widetilde{\rho}}].\end{cases} \tag{13}$$

Similarly, the numerical flux $G_{i,j+1/2}$ can be constructed as well. With the above numerical fluxes at the cell interface, the flow variables inside each deforming control volume can be updated.

3.2. High-order multidimensional fluxes

In this subsection, a high-order multidimensional gas-kinetic solver will be presented based on the high-order initial reconstruction which will be given in the next subsection.

With the reconstructed quadratic polynomials for the flow variables, a time-dependent gas distribution function will be constructed at a cell interface. The integral solution of BGK equation (10) at the cell interface can be written as

$$f(\xi_{i+1/2},\eta,t,\widetilde{u},\widetilde{v},\varsigma)=\frac{1}{\tau}\int_0^t g(\xi',\eta',t',\widetilde{u},\widetilde{v},\varsigma)e^{-(t-t')/\tau}dt'+e^{-t/\tau}f_0(-\widetilde{u}t,\eta-\widetilde{v}t,\widetilde{u},\widetilde{v},\varsigma), \tag{14}$$

where $\xi_{i+1/2}=0$ is the location of the cell interface, $\xi_{i+1/2}=\xi'+\widetilde{u}(t-t')$ and $\eta=\eta'+\widetilde{v}(t-t')$ are the trajectory of particles, f_0 is the initial gas distribution function and g is the corresponding equilibrium state.

To construct a high-order multidimensional gas-kinetic solver, the following notations are introduced firstly

$$a_1 = (\partial g/\partial\xi)/g, a_2 = (\partial g/\partial\eta)/g, \Lambda = (\partial g/\partial t)/g,$$
$$d_{11} = (\partial a_1/\partial\xi), d_{12} = (\partial a_1/\partial\eta) = (\partial a_2/\partial\xi), d_{22} = (\partial a_2/\partial\eta),$$
$$b_1 = (\partial a_1/\partial t) = (\partial\Lambda/\partial\xi), b_2 = (\partial a_2/\partial t) = (\partial\Lambda/\partial\eta), \Gamma = (\partial\Lambda/\partial t),$$

where g is an equilibrium state. The dependence of these coefficients on the particle velocity can be obtained from the Taylor expansion of a Maxwellian and has the following form

$$a_1 = a_{11} + a_{12}\widetilde{u} + a_{13}\widetilde{v} + a_{14}\frac{1}{2}(\widetilde{u}^2 + \widetilde{v}^2 + \varsigma^2),$$
$$\dots$$
$$\Gamma = \Gamma_1 + \Gamma_2\widetilde{u} + \Gamma_3\widetilde{v} + \Gamma_4\frac{1}{2}(\widetilde{u}^2 + \widetilde{v}^2 + \varsigma^2).$$

To high-order accuracy, the Taylor expansion for the initial gas distribution function at $(\xi,\eta) = (0,0)$ is expressed as

$$f_0(\xi,\eta,\widetilde{u},\widetilde{v},\varsigma) = f_G + \frac{\partial f_G}{\partial\xi}\xi + \frac{\partial f_G}{\partial\eta}\eta + \frac{1}{2}\frac{\partial^2 f_G}{\partial\xi^2}\xi^2 + \frac{\partial^2 f_G}{\partial\xi\partial\eta}\xi\eta + \frac{1}{2}\frac{\partial^2 f_G}{\partial\eta^2}\eta^2,$$

where f_G is the distribution function, which is $f_{G,E} = g$ for the Euler solutions, and $f_{G,NS} = g - \tau(\widetilde{u}g_\xi + \widetilde{v}g_\eta + g_t)$ for the Navier–Stokes solutions.

With the reconstructed quadratic polynomial, which will be introduced in next subsection, the initial Navier–Stokes gas distribution function on both sides of a cell interface can be expressed as

$$f_0 = \begin{cases} f_0^l(\xi,\eta,\widetilde{u},\widetilde{v},\varsigma), \xi < 0, \\ f_0^r(\xi,\eta,\widetilde{u},\widetilde{v},\varsigma), \xi > 0, \end{cases} \tag{15}$$

where f_0^l and f_0^r are the third-order Taylor expansion for $f_{G,NS}^l$ and $f_{G,NS}^r$. When $f_0^{l,r}$ takes the form of $f_{G,E}^{l,r}$, the expansion corresponds to the Euler solutions.

After determining f_0, the equilibrium state g can be constructed with spatial and temporal accuracy being consistent with the expansion of f_0

$$\begin{aligned} g = g_0 &+ \frac{\partial g_0}{\partial\xi}\xi + \frac{\partial g_0}{\partial\eta}\eta + \frac{\partial g_0}{\partial t}t + \frac{1}{2}\frac{\partial^2 g_0}{\partial\xi^2}\xi^2 + \frac{1}{2}\frac{\partial^2 g_0}{\partial\eta^2}\eta^2 \\ &+ \frac{1}{2}\frac{\partial^2 g_0}{\partial t^2}t^2 + \frac{\partial^2 g_0}{\partial\xi\partial\eta}\xi\eta + \frac{\partial^2 g_0}{\partial\xi\partial t}\xi t + \frac{\partial^2 g_0}{\partial\eta\partial t}\eta t, \end{aligned} \tag{16}$$

where g_0 is the equilibrium state located at the interface, which can be determined through the compatibility condition (5)

$$\iint \widetilde{\psi} g_0 d\widetilde{\Xi} = W_0 = \iint_{\widetilde{u}>0} \widetilde{\psi} g_l d\widetilde{\Xi} + \iint_{\widetilde{u}<0} \widetilde{\psi} g_r d\widetilde{\Xi}, \tag{17}$$

where g_l, g_r are the corresponding equilibrium states at both side of the cell interface.

Substituting Eq. (15) and Eq. (16) into the integral solution (14), the gas distribution function at cell interfaces can be fully determined, where

$$\begin{aligned} &\frac{1}{\tau}\int_0^t g\,(\xi',\eta',t',\widetilde{u},\widetilde{v},\varsigma)e^{-(t-t')/\tau}dt' \\ &= C_1 g_0 + C_2 g_0\bar{a}_1\widetilde{u} + C_2 g_0\bar{a}_2\widetilde{v} + C_3 g_0\overline{\Lambda} \\ &+ \frac{1}{2}C_4 g_0(\bar{a}_1^2 + \bar{d}_{11})\widetilde{u}^2 + C_2 g_0(\bar{a}_1\bar{a}_2 + \bar{d}_{12})\widetilde{u}\eta + C_4 g_0(\bar{a}_1\bar{a}_2 + \bar{d}_{12})\widetilde{u}\widetilde{v} \\ &+ \frac{1}{2}C_1 g_0(\bar{a}_2^2 + \bar{d}_{22})\eta^2 + C_2 g_0(\bar{a}_2^2 + \bar{d}_{22})\widetilde{v}\eta + \frac{1}{2}C_4 g_0(\bar{a}_2^2 + \bar{d}_{22})\widetilde{v}^2 \\ &+ C_6 g_0(\overline{\Lambda}\bar{a}_1 + \bar{b}_1)\widetilde{u} + C_3 g_0(\overline{\Lambda}\bar{a}_2 + \bar{b}_2)\eta + C_6 g_0(\overline{\Lambda}\bar{a}_2 + \bar{b}_2)\widetilde{v} + \frac{1}{2}C_5 g_0(\overline{\Lambda}^2 + \overline{\Gamma}), \end{aligned} \tag{18}$$

and the coefficients $\bar{a}_1, \bar{a}_2, \dots, \overline{\Lambda}, \overline{\Gamma}$ are corresponding to the equilibrium state g_0 in Eq. (16). For the kinetic part, we have

$$f_0(-\widetilde{u}t, \eta - \widetilde{v}t, \widetilde{u}, \widetilde{v}, \varsigma) = f_0^l(-\widetilde{u}t, \eta - \widetilde{v}t, \widetilde{u}, \widetilde{v}, \varsigma)H(\widetilde{u}) + f_0^r(-\widetilde{u}t, \eta - \widetilde{v}t', \widetilde{u}, \widetilde{v}, \varsigma)(1 - H(\widetilde{u})),$$

where

$$
\begin{aligned}
&e^{-t/\tau} f_0^k(-\widetilde{u}t, \eta-\widetilde{v}t, \widetilde{u}, \widetilde{v}, \varsigma)\\
&\quad = C_7 g_k[1-\tau(a_{1k}\widetilde{u}+a_{2k}\widetilde{v}+\Lambda_k)]\\
&\quad + C_8 g_k[a_{1k}\widetilde{u}-\tau((a_{1k}^2+d_{11k})\widetilde{u}^2+(a_{1k}a_{2k}+d_{12k})\widetilde{u}\widetilde{v}+(\Lambda_k a_{1k}+b_{1k})\widetilde{u})]\\
&\quad + C_8 g_k[a_{2k}\widetilde{v}-\tau((a_{1k}a_{2k}+d_{12k})\widetilde{u}\widetilde{v}+(a_{2k}^2+d_{22k})\widetilde{v}^2+(\Lambda_k a_{2k}+b_{2k})\widetilde{v})]\\
&\quad + C_7 g_k[a_{2k}-\tau((a_{1k}a_{2k}+d_{12k})\widetilde{u}+(a_{2k}^2+d_{22k})\widetilde{v}+(\Lambda_k a_{2k}+b_{2k}))]\eta\\
&\quad + \frac{1}{2}C_9 g_k(a_{1k}^2+d_{11k})\widetilde{u}^2+\frac{1}{2}C_7 g_k(a_{2k}^2+d_{22k})\eta^2+\frac{1}{2}C_9 g_k(a_{2k}^2+d_{22k})\widetilde{v}^2\\
&\quad + C_9 g_k(a_{2k}^2+d_{22k})\widetilde{v}\eta+C_9 g_k(a_{1k}a_{2k}+d_{12k})\widetilde{u}\eta+C_9 g_k(a_{1k}a_{2k}+d_{12k})\widetilde{u}\widetilde{v},
\end{aligned}
\tag{19}
$$

where the coefficients $a_{1k}, a_{2k}, \ldots, \Lambda_k$ are corresponding to the equilibrium state g_k in Eq. (16), $k = l, r$. The coefficients $C_i, i = 1, \ldots, 9$ are given by

$$
\begin{aligned}
&C_1 = 1-e^{-t/\tau}, C_2 = (t+\tau)e^{-t/\tau}-\tau, C_3 = t-\tau+\tau e^{-t/\tau}, C_4 = -(t^2+2t\tau)e^{-t/\tau},\\
&C_5 = t^2-2t\tau, C_6 = -t\tau(1+e^{-t/\tau}), C_7 = e^{-t/\tau}, C_8 = -te^{-t/\tau}, C_9 = t^2e^{-t/\tau}.
\end{aligned}
$$

The superscripts or subscripts of the coefficients $a_1, a_2, \ldots, \Gamma, \Lambda$ in Eq. (18) and Eq. (19) are omitted for simplicity and they are determined by the spatial derivatives of macroscopic flow variables and the compatibility condition [22,27] as follows

$$
\begin{cases}
\langle a_1\rangle = \dfrac{\partial W}{\partial \xi}, \langle a_2\rangle = \dfrac{\partial W}{\partial \eta}, \langle \Lambda + a_1\widetilde{u}+a_2\widetilde{v}\rangle = 0,\\
\langle a_1^2+d_{11}\rangle = \dfrac{\partial^2 W}{\partial \xi^2}, \langle a_2^2+d_{22}\rangle = \dfrac{\partial^2 W}{\partial \eta^2}, \langle a_1a_2+d_{12}\rangle = \dfrac{\partial^2 W}{\partial \xi\partial\eta},\\
\langle (a_1^2+d_{11})\widetilde{u}+(a_1a_2+d_{12})\widetilde{v}+(\Lambda a_1+b_1)\rangle = 0,\\
\langle (a_1a_2+d_{12})\widetilde{u}+(a_2^2+d_{22})\widetilde{v}+(\Lambda a_2+b_2)\rangle = 0,\\
\langle (\Lambda a_1+b_1)\widetilde{u}+(\Lambda a_2+b_2)\widetilde{v}+(\Lambda^2+\Gamma)\rangle = 0,
\end{cases}
\tag{20}
$$

where W is the projected conservative variables, and $\langle \ldots \rangle$ are the moments of corresponding variables and defined as

$$
\langle \ldots \rangle = \int g(\ldots)\widetilde{\psi} d\widetilde{\Xi},
$$

$\widetilde{\psi} = (1, \widetilde{u}, \widetilde{v}, \frac{1}{2}(\widetilde{u}^2+\widetilde{v}^2+\varsigma^2))$. Substituting Eq. (14) into Eq. (12), the numerical flux across the cell interface in the inertial frame can be obtained.

3.3. Reconstruction

The above time evolution solution is based on the high-order initial reconstruction for macroscopic flow variables. For the initial reconstruction, the fifth-order WENO scheme [23,15] is adopted to determine the cell interface discontinuities.

To construct the initial distribution f_0, the corresponding polynomial for the conservative flow variables in the normal direction are obtained as follows. With the cell averaged value W_i and the reconstructed variables at two ends of each cell W_i^r and W_i^l, a third-order polynomial inside each cell can be obtained as follows

$$
W_i(\xi) = W_i + (\frac{\partial W}{\partial \xi})_i(\xi-\xi_i) + \frac{1}{2}(\frac{\partial^2 W}{\partial \xi^2})_i[(\xi-\xi_i)^2 - \frac{1}{12}\Delta\xi^2],
$$

where $\xi \in [\xi_{i-1/2}, \xi_{i+1/2}]$. The first and second order normal derivatives at the cell interface can be determined from the above polynomial. Based on the WENO reconstruction of $W_{i,j-k}^r, W_{i+1,j-k}^l, k = -2, \ldots, 2$ on the tangential direction, the tangential and cross derivative terms can be also obtained on both sides of cell interface. With the reconstructed polynomials on both sides of the cell interface $W_i(\xi), W_{i+1}(\xi)$, the coefficients $a_{1k}, a_{2k}, \ldots, \Lambda_k, k = l, r$ in Eq. (19) can be determined according to Eq. (20).

To determine the equilibrium state g across the cell interface, the conservative variables around the cell interface in the normal direction can be expanded as

$$
\overline{W}(\xi) = W_0 + S_i^1(\xi-\xi_i) + \frac{1}{2}S_i^2(\xi-\xi_i)^2 + \frac{1}{6}S_i^3(\xi-\xi_i)^3 + \frac{1}{24}S_i^4(\xi-\xi_i)^4,
$$

where W_0 is the conservative variables corresponding to the equilibrium state g at the cell interface according to the compatibility condition (17). With the following conditions

$$
\int_{I_{i+k}} \overline{W}(\xi) = W_{i+k}, k = -1, \ldots, 2,
$$

the polynomial $\overline{W}(\xi)$ can be fully determined. The tangential and cross derivatives can be constructed based on the WENO reconstruction of $W_{0,j-k}, k=-2,\ldots,2$ on the tangential direction along the cell interface. With the polynomials $\overline{W}(\xi)$ across the cell interface, the coefficients $\bar{a}_1, \bar{a}_2, \ldots, \overline{\Lambda}, \overline{\Gamma}$ in Eq. (18) can be also determined according to Eq. (20).

For the smooth flow, the third-order reconstruction can be adopted directly in the computation. The polynomials at both sides of cell interface take the same $\overline{W}(\xi)$, which gives $g_0 = g_l = g_r$ and identical slopes. Consequently, the gas distribution function (14) will reduce to the continuous one [27]. The above scheme can be readily extended to three-dimensional flow computation [18].

3.4. Gas-kinetic scheme with mesh velocity and acceleration

In this subsection, both mesh velocity (U_g, V_g) and acceleration (a, b) will be included in the scheme construction. By projecting the relative velocity and acceleration in the normal direction **n** and tangential direction **t** and according to the notations introduced following Eq. (10), the BGK equation with both mesh velocity and acceleration (6) can be written as

$$\frac{\partial f}{\partial t} + \frac{\partial(\widetilde{u} f)}{\partial \xi} + \frac{\partial(\widetilde{v} f)}{\partial \eta} - \widetilde{\alpha}\frac{\partial f}{\partial \widetilde{u}} - \widetilde{\beta}\frac{\partial f}{\partial \widetilde{v}} = \frac{g - f}{\tau}, \tag{21}$$

where $\widetilde{\alpha} = (aM - bL)/S$ and $\widetilde{\beta} = (aL + bM)/S$ are the corresponding mesh accelerations.

For simple presentation, the directional-splitting flux will be given in this subsection. The integral solution with acceleration at the cell interface [35] can be written as

$$f(\xi_{i+1/2}, t, \widetilde{u}, \widetilde{v}, \varsigma) = \frac{1}{\tau}\int_0^t g(\xi', t', \widetilde{u}, \widetilde{v}, \varsigma) e^{-(t-t')/\tau} dt' + e^{-t/\tau} f_0(\xi_{i+1/2} - \widetilde{u}t), \tag{22}$$

where $\xi_{i+1/2} = \xi' + \widetilde{u}'(t-t') - \frac{1}{2}\widetilde{\alpha}(t-t)^2$ and $\widetilde{u} = \widetilde{u}' - \widetilde{\alpha}(t-t')$.

Because of the acceleration, the particle velocity change needs to be included, as well as the modification of the equilibrium gas distribution function along the trajectory. Suppose that a particle moves from ξ' to ξ in a short time interval $t-t'$, the particle velocity will change from to u' to $u = u' - \widetilde{\alpha}(t-t')$. So due to the particle velocity change, an equilibrium state g_0 at time t' can be expressed as

$$\begin{aligned} g_0(x', t', \widetilde{u}', \widetilde{v}, \varsigma) &= \rho(\frac{\lambda}{\pi})^{\frac{K+2}{2}} e^{-\lambda[(\widetilde{u}'-\widetilde{U})^2 + (\widetilde{v}-\widetilde{V})^2 + \varsigma^2]} \\ &= \rho(\frac{\lambda}{\pi})^{\frac{K+2}{2}} e^{-\lambda[(\widetilde{u}-\widetilde{U})^2 + (\widetilde{v}-\widetilde{V})^2 + \varsigma^2]} e^{-\lambda[2(\widetilde{u}-\widetilde{U})\widetilde{\alpha}(t-t') + \widetilde{\alpha}(t-t')^2]} \\ &= g \cdot e^{\lambda[-2(\widetilde{u}-\widetilde{U})\widetilde{\alpha}(t-t') - \widetilde{\alpha}(t-t')^2]}, \end{aligned}$$

where g is the equilibrium state at time t. Using the Taylor expansion and neglecting the $(t-t')^2$ order term, the above equilibrium state can be expressed as

$$g_0(x', t', u', \varsigma) \simeq g[1 - 2\lambda\widetilde{\alpha}(\widetilde{u} - \widetilde{U})(t-t')]. \tag{23}$$

Based on the reconstructed data and the modified equilibrium state (23), the distribution function (22) can be fully determined.

Because of the acceleration, the relationship between particle velocity u, v in the inertia reference of frame and $\widetilde{u}, \widetilde{v}$ in the moving reference of frame needs to be modified, and we have

$$\begin{cases} u = U_g + (M\widetilde{u} + L\widetilde{v})/S + at, \\ v = V_g + (-L\widetilde{u} + M\widetilde{v})/S + bt. \end{cases} \tag{24}$$

where U_g, V_g and a, b are constant within each time step in the computation, and $t \in [0, \Delta t]$.

Substituting Eq. (24) into Eq. (12), the numerical fluxes in the inertia frame of reference $F_{i+1/2,j} = (F_\rho, F_m, F_n, F_E)$ can be obtained

$$\begin{cases} F_\rho = SF_{\widetilde{\rho}}, \\ F_m = SU_g F_{\widetilde{\rho}} + SatF_{\widetilde{\rho}} + (MF_{\widetilde{\rho u}} + LF_{\widetilde{\rho v}}), \\ F_n = SV_g F_{\widetilde{\rho}} + SbtF_{\widetilde{\rho}} + (-LF_{\widetilde{\rho u}} + MF_{\widetilde{\rho v}}), \\ F_E = SF_{\widetilde{E}} + \dfrac{S}{2}[(U_g^2 + V_g^2)F_{\widetilde{\rho}} + 2(U_g a + V_g b)tF_{\widetilde{\rho}} + (a^2 + b^2)t^2 F_{\widetilde{\rho}}] \\ \quad + [(MU_g - LV_g)F_{\widetilde{\rho u}} + (LU_g + MV_g)F_{\widetilde{\rho v}}] + [(Ma - Lb)tF_{\widetilde{\rho u}} + (La + Mb)tF_{\widetilde{\rho v}}], \end{cases} \tag{25}$$

where $F_{\widetilde{\rho}}, F_{\widetilde{\rho u}}, F_{\widetilde{\rho v}}, F_{\widetilde{E}}$ are the numerical fluxes standing on a moving cell interface, which are obtained by taking moments of the time dependent gas distribution function in Eq. (22). Together with the numerical fluxes $G_{i,j+1/2}$ in η direction, the flow variables inside each deforming control volume can be updated according to Eq. (7).

3.5. Numerical procedures

The numerical procedure of the moving-mesh gas-kinetic scheme can be summarized as follows:

1. Set the initial cell averaged $(\rho, \rho U, \rho V, \rho E)$ and the geometric variables (A, B, M, L) at each cell center by Eq. (2). Then, $(\Delta\rho, \Delta\rho U, \Delta\rho V, \Delta\rho E)$ are calculated for each control volume with $\Delta = AM - BL$.
2. According to the given mesh velocity (U_g, V_g) at the cell interface $\xi = \xi_{i+1/2}$, project the flow variables to the local coordinate by Eq. (9). The high-order reconstruction is conducted for the projected conservative variables W around the cell interface in both normal and tangential directions.
3. With reconstructed data, calculate the numerical fluxes on the moving interface by taking moments of the gas distribution function (14) (without mesh acceleration) or Eq. (22) (with mesh acceleration), and obtain the numerical fluxes in the common inertia frame of reference according to Eq. (13) (without mesh acceleration) or Eq. (25) (with mesh acceleration).
4. Generate the new mesh according to the mesh velocity at $t = t^{n+1}$

$$x_{i,j}^{n+1} = x_{i,j}^{n} + U_g \Delta t^n + \frac{1}{2} a \left(\Delta t^n\right)^2,$$
$$y_{i,j}^{n+1} = y_{i,j}^{n} + V_g \Delta t^n + \frac{1}{2} b \left(\Delta t^n\right)^2,$$

   where U_g, V_g and a, b are constant within each time step, $\Delta t^n = t^{n+1} - t^n$. If there is no mesh acceleration, both a and b take the value of 0. With the new mesh, (A, B, L, M) and Δ are calculated, such as $A_{i,j}^{n+1}$,

$$A_{i,j}^{n+1} = \left(x_{i+1/2,j}^{n+1} - x_{i-1/2,j}^{n+1}\right)/\Delta\xi.$$

5. Updated the conservative variables at $t = t^{n+1}$ by the finite volume scheme (7) with the fluxes in the inertia frame of reference.
6. Repeat steps 2 to 5 until the computation stops.

4. Numerical tests

In this section, numerical tests for both inviscid and viscous flow will be presented to validate the scheme. For the inviscid flow, the collision time τ takes

$$\tau = \epsilon \Delta t + C \left| \frac{p_l - p_r}{p_l + p_r} \right| \Delta t,$$

where, in this paper, $\varepsilon = 0.01$ and $C = 1$. For the viscous flow, the local particle collision time is determined by

$$\tau = \frac{\mu}{p} + C \left| \frac{p_l - p_r}{p_l + p_r} \right| \Delta t,$$

where p_l, p_r denotes the pressures on the left and right hand sides of a cell interface. Here μ is the dynamic viscous coefficient, p is the pressure of the equilibrium state at the cell interface, and C also takes 1. For smooth flow, it will reduce to $\tau = \frac{\mu}{p}$. The time step Δt is determined according to the CFL condition, and CFL number takes a value of 0.2 in the current computations.

The multi-dimensional flux is used for the cases without considering acceleration, and the dimensional-splitting flux is only used in the simple wave case.

4.1. Shock tube problem

In this case, we consider the one-dimensional Lax shock tube problem. The initial conditions are given as follows

$$\begin{cases} (\rho, u, p) = (0.445, 1.198, 3.528), & 0 \le x < 0.5 \\ (\rho, u, p) = (0.5, 0.5, 0.571), & 0.5 \le x \le 1. \end{cases}$$

The mesh moves with grid velocity $U_g = 0.5$, uniformly. In the computation, the 100×10 mesh is used, which represents the initial domain $[0, 1] \times [0, 0.1]$. Non-reflecting boundary conditions are used in the x and y directions. The distribution of density, relative velocity, and pressure of the current scheme at $t = 0.1$ are presented in Fig. 1 at fixed $y = 0.05$. Because of mesh velocity, the initial physical domain moves to $[0.05, 1.05] \times [0, 0.1]$ at $t = 0.1$. The exact solution of the Lax problem is obtained without considering mesh movement. The numerical results agree well with the exact solution.

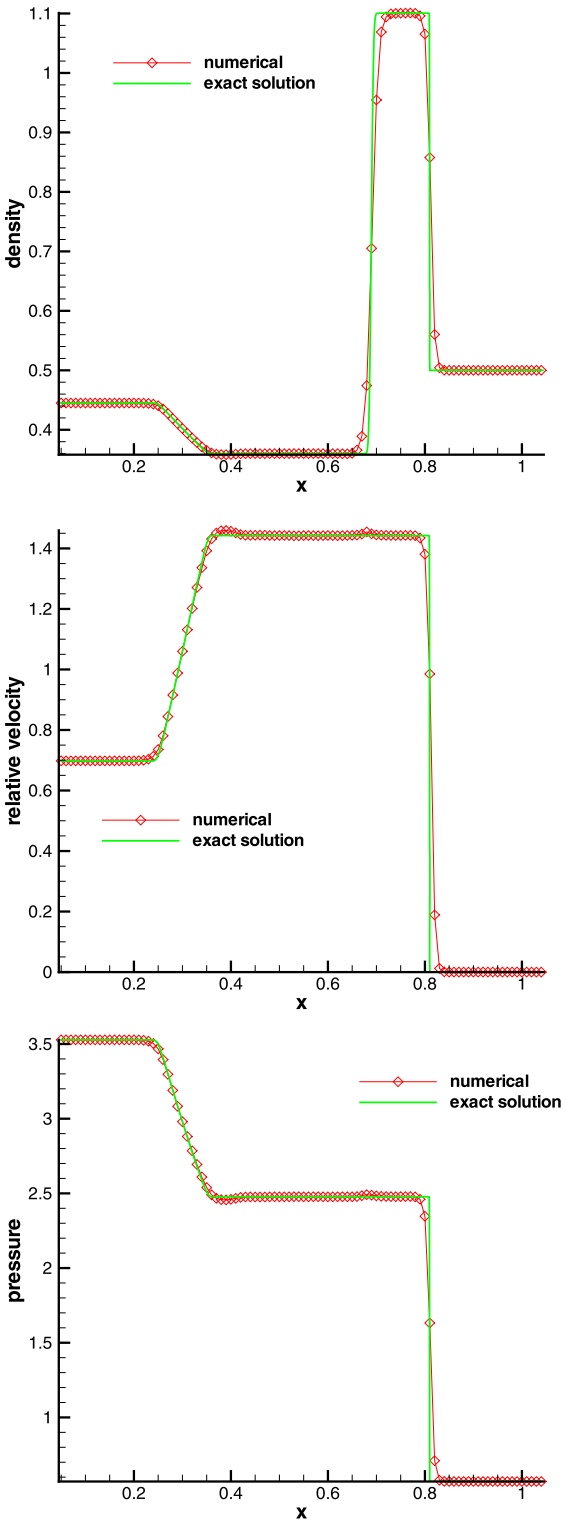

Fig. 1. Lax problem: density, relative velocity, and pressure distributions at $t = 0.1$ with 100 cells. Diamonds: moving-mesh scheme. Green line: exact solution. (For interpretation of the references to color in this figure legend, the reader is referred to the web version of this article.)

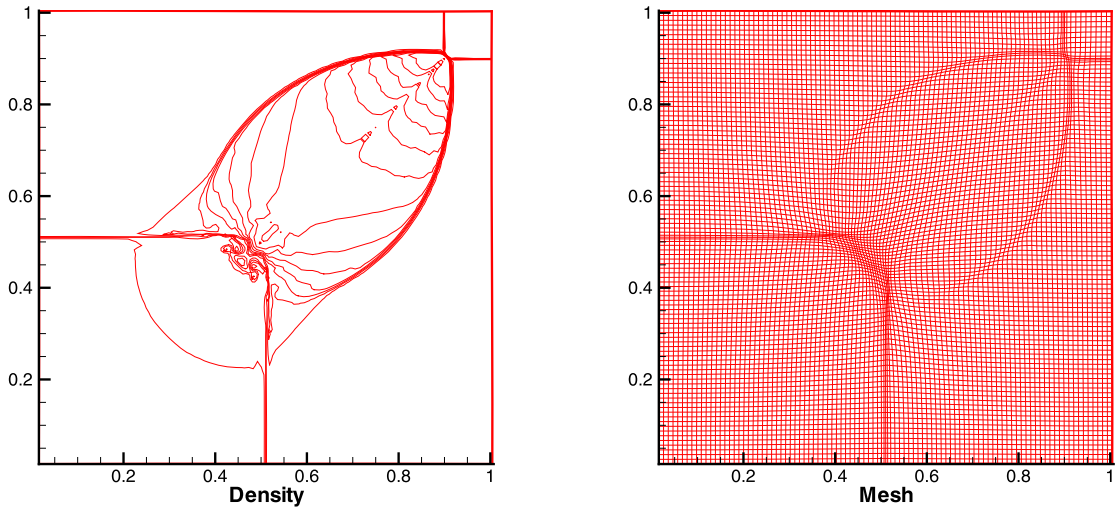

Fig. 2. The density contour and mesh for the first 2D Riemann problem at $t = 0.25$.

4.2. Two-dimensional Riemann problem

In this case, two 2D Riemann problems are tested. Both of these two cases were presented in [24]. The initial condition for the first problem is

$$(\rho, u, v, p) = \begin{cases} (0.5313, 0, 0, 0.4), & x > 0.5, y > 0.5, \\ (1, 0.7276, 0, 1), & x < 0.5, y > 0.5, \\ (0.8, 0, 0, 1), & x > 0.5, y < 0.5, \\ (1, 0, 0.7276, 1), & x > 0.5, y < 0.5. \end{cases}$$

The initial condition for second case is

$$(\rho, u, v, p) = \begin{cases} (1, 0.1, 0.1, 1), & x > 0.5, y > 0.5, \\ (0.5197, -0.6259, 0.1, 0.4), & x < 0.5, y > 0.5, \\ (0.8, 0.1, 0.1, 0.4), & x > 0.5, y < 0.5, \\ (0.5197, 0.1, -0.6259, 0.4), & x > 0.5, y < 0.5. \end{cases}$$

Initially 100×100 uniform mesh, which covers the domain $[0, 1] \times [0, 1]$, is used for both cases. Non-reflecting boundary conditions are used in the x and y directions. The mesh velocity is determined by solving an elliptic solver, which is equivalent to optimizing some function [31]. The monitor function ω_m takes

$$\omega_m = \sqrt{1 + 0.1(|\nabla \rho|^2 + |\nabla \mathbf{u}|^2)}.$$

Assume that the new mesh is obtained at the $n+1$-th time step, the mesh velocity $\mathbf{U}_g$ can be determined as follows

$$\mathbf{U}_g = \frac{\mathbf{X}_{ij}^{n+1} - \mathbf{X}_{ij}^{n}}{\Delta t},$$

where $\mathbf{X}_{ij}^{n}$ are the coordinates of the mesh points and Δt is the time step. This choice of mesh velocity can be considered as an adaptive mesh method. Different from the Lagrangian method, based on the different monitor functions, a smooth mesh can be obtained. At the same time, the mesh can be automatically concentrated in the regions with high gradients of physical variables, which improve the solution accuracy substantially. Both the density contours and computational mesh of these two cases at $t = 0.25$ are presented in Fig. 2 and Fig. 3. The current results agree well with those in [24]. Especially, due to the high-order and multi-dimensionality of the solver, and the adaptive mesh moving procedure, the roll-up can be captured effectively in the second case.

4.3. Flow over NACA 0012 airfoil

This case is about the inviscid flow computation of transonic flow passing through a NACA 0012 airfoil. The initial angle of attack is $\alpha_m = 0.016^\circ$. Around a point on the chord, which is located at the chord with a quarter of chord length from the leading point, the airfoil is oscillating and the cycle of oscillation is defined as

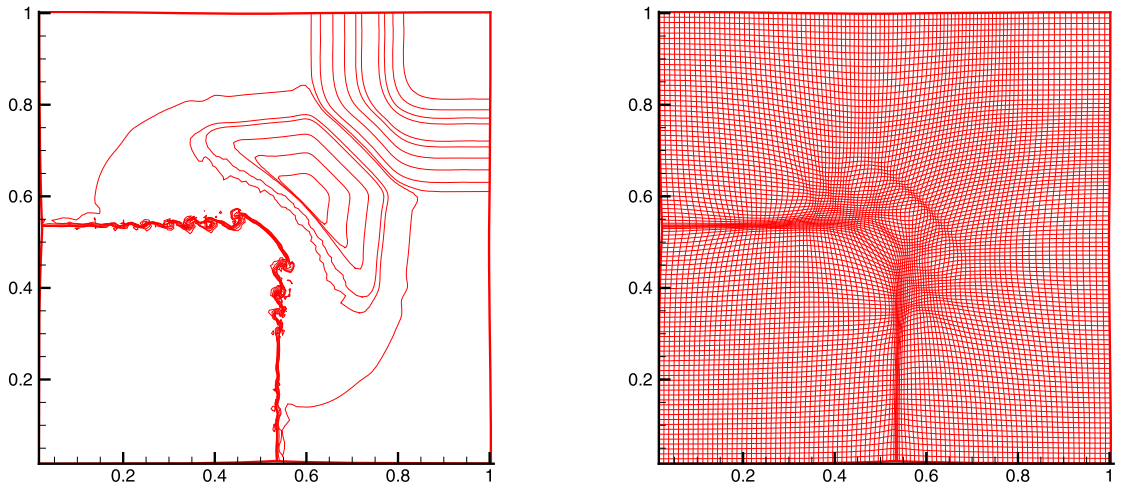

Fig. 3. The density contour and mesh for the second 2D Riemann problem at $t = 0.25$.

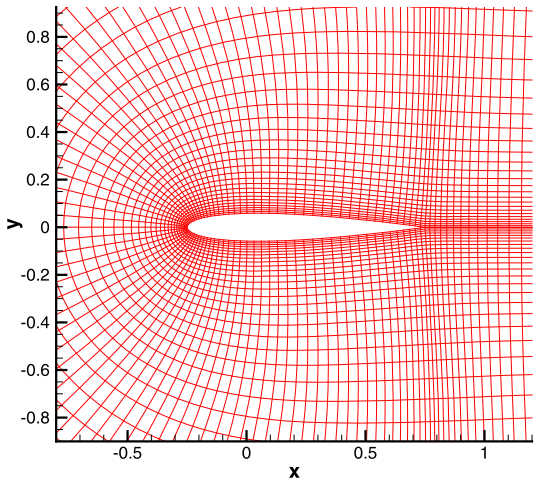

Fig. 4. The initial mesh of NACA 0012 airfoil.

$$\alpha = \alpha_m + \alpha_0 \sin \omega t,$$

where ω is the frequency and $\alpha_0 = 2.51°$.

With the above settings, the angular velocity ω around this point is given. In the computation, the whole mesh around the airfoil moves with the angular velocity. A 178×44 mesh points are used in the computation. The initial computational mesh is presented in Fig. 4, which is a C-type structured mesh. The inviscid boundary condition is used on the surface of the airfoil, and the inflow and outflow boundary conditions are used in the inlet and outlet respectively. The free stream velocity U_∞ with a Mach number 0.755 is fixed and parallel to the x-axis, and the reduced frequency $\omega c/2U_\infty = 0.0814$. The density and pressure distributions at $\omega t = 4\pi$ are presented in Fig. 5. The pressure distribution at the angles of attack $-2.0°$ and $-0.54°$ are given in Fig. 6, with the inclusion of experiment measurements. The numerical results agree well with the experiment data [21].

4.4. Viscous flow above an oscillating wall

This case is so-called Stokes' second problem which describes fluid motion above a flat plate which executes sinusoidal oscillations parallel to itself, and the flow is dominated by the viscous shear. The governing equation for the U velocity in the y-direction is

$$\frac{\partial U}{\partial t} = \nu \frac{\partial^2 U}{\partial y^2}, \tag{26}$$

with the boundary conditions

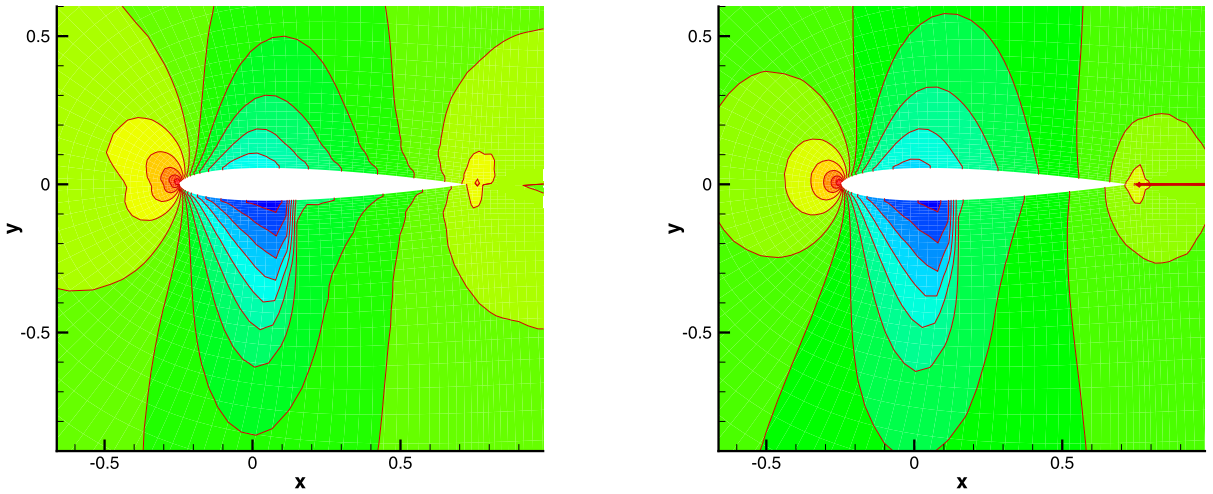

Fig. 5. The distribution of density and pressure around a NACA 0012 airfoil at $\omega t = 4\pi$. The left one is the density contour and the right one is the pressure contour.

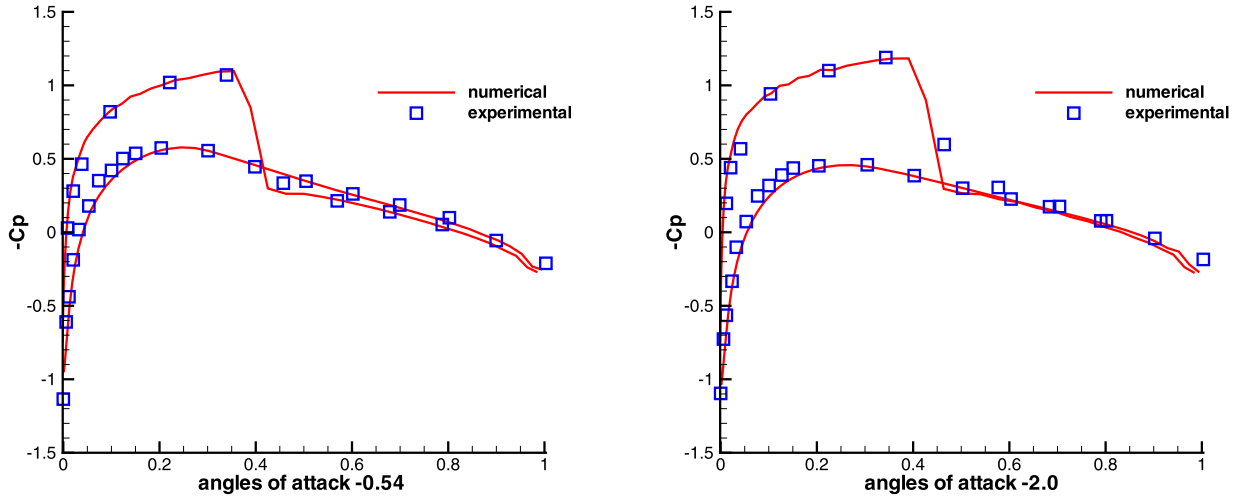

Fig. 6. Pressure distributions on the surface of NACA 0012 airfoil at the angles of attack $-2.0°$ and $-0.54°$.

$$U(0,t) = U_0 cos(\omega t), \quad U(\infty,t) = 0.$$

The exact solution of this problem is

$$U(y,t) = U_0 e^{-y\sqrt{\omega/2\nu}} cos(\omega t - y\sqrt{\omega/2\nu}),$$

where ν is viscosity coefficient.

The initial flow field is stationary with $\rho = 1, p = 1/\gamma Ma^2, \gamma = 5/3$, $\nu = 0.0005$ and $\omega = 0.1$. To simulate this problem, the Mach number takes a small value of $Ma = 0.15$. The non-slip adiabatic boundary condition at the plate, the non-reflecting boundary condition at top boundary and the periodic boundary condition in the x direction are adopted. The 10×10, 10×20 and 10×40 meshes are used in the computations for the initial domain $[0, 0.1] \times [0, 0.8]$ and the mesh moves with the velocity $(U_g, V_g) = (U_{wall}, 0)$ uniformly. The mesh could also move with the fluid velocity and it will become a Lagrangian method. However, because of the large velocity shear, the mesh will be stretched severely. The initial mesh and the numerical results and exact solutions of velocity at $\omega t = 2.5\pi, 5\pi$ are presented in Fig. 7. Good mesh convergence is achieved. The velocity profile can be satisfactorily obtained even with 2 to 3 mesh points in the boundary layer due to the third-order accuracy of the current scheme. This case will be difficult for the high-order schemes based on the Riemann solvers.

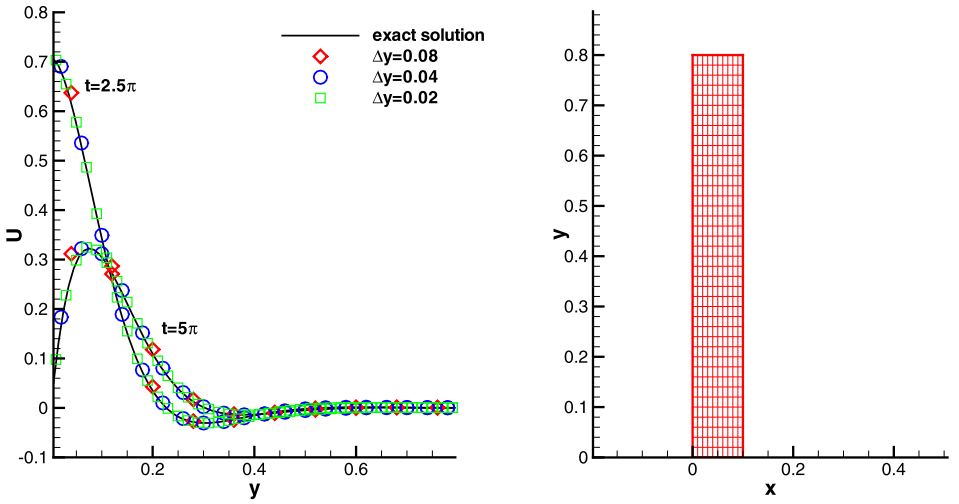

Fig. 7. The velocity profiles and mesh for an oscillating wall. The velocity profiles with different cell size, where the solid lines are the exact solutions and symbols represent the numerical results (left); the initial mesh with $\Delta x = 0.01$ and $\Delta y = 0.02$ (right).

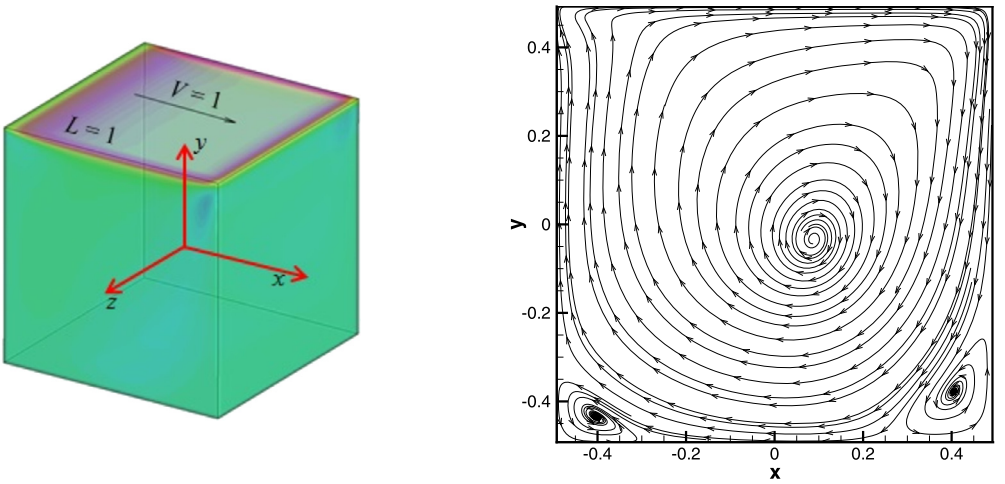

Fig. 8. The geometry of three-dimensional cavity flow (left); the stream lines with 65×65 mesh for three-dimensional cavity flow in the x–y plane at $z = 0$ (right).

4.5. Three-dimensional cavity flow

The lid-driven-cavity problem is one of the most important benchmarks for Navier–Stokes solvers, where the fluid is bounded by a unit cubic and driven by a uniform translation of the top boundary as shown in Fig. 8 and the domain is $[-0.5, 0.5] \times [-0.5, 0.5] \times [-0.5, 0.5]$. This case is used to validate three-dimensional scheme with the stationary mesh. Early three-dimensional cavity-flow calculations were carried out by De Vahl Davis and Mallinson [7] and Goda [10]. In this case, the flow is simulated with Mach number $Ma = 0.15$ at Reynolds number $Re = 1000$ and all boundaries are isothermal and nonslip. The computation is conducted with $65 \times 65 \times 65$ mesh points inside the cubic. The stream lines in the x–y plane at $z = 0$ are presented in Fig. 8. The results of U-velocity along the vertical centerline line, V-velocity along the horizontal centerline in the x–y plane with $z = 0$ and the benchmark data [1] are shown in Fig. 9. The simulation results match well with the benchmark data. This test shows that the high-order gas-kinetic scheme is very effective to simulate complicated three-dimensional flow. The current accuracy can be hardly achieved from a high-order directional splitting method. As a reference, the CPU time for this case with $65 \times 65 \times 65$ points and 100 time steps is 315.364 seconds for single core of Intel Core i7-4770 CPU @ 3.40 GHz; meanwhile, the CPU time for 2D cavity flow with 65×65 points and 100 time steps is 1.985 seconds for the same machine.

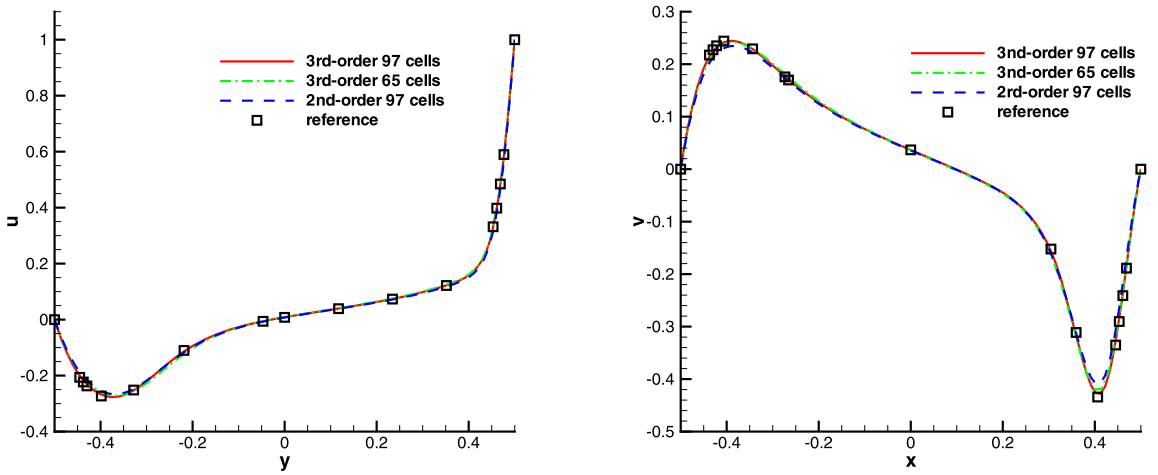

Fig. 9. The profiles of U-velocity along the vertical centerline line (left) and V-velocity along the horizontal centerline (right) in the x–y plane at $z = 0$. The reference data is taken from Albensoeder [1].

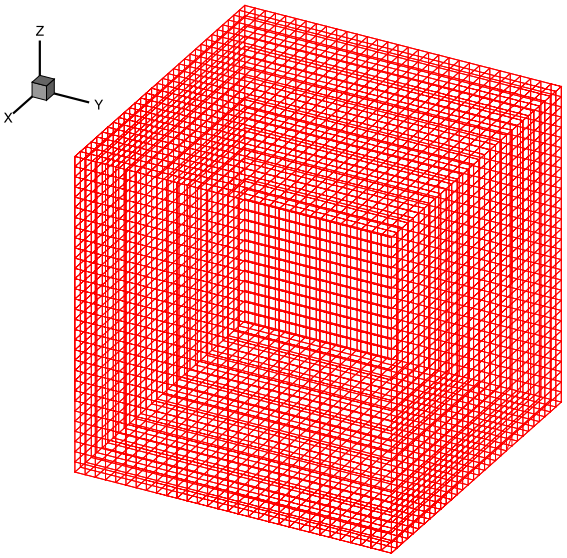

Fig. 10. The initial mesh for the 3D rotating cavity.

4.6. Flow inside a three-dimensional rotating cavity

In this case, the flow inside a rotating unit cubic cavity is studied. The rotating angular velocity is $\omega = 1$ around z-axis. With the account of the largest speed at the cavity wall corresponding to a Mach number 0.1, the viscosity coefficient is determined by requiring the Reynolds number $Re = 1000$. At the beginning, the flow is stationary and it starts to move due to the viscous effect from the cavity wall. The third-order reconstruction is adopted in this case. The initial mesh is presented in Fig. 10, where $33 \times 33 \times 33$ uniform mesh is used to represent the initial domain of $[-0.5, 0.5] \times [-0.5, 0.5] \times [-0.5.0.5]$, and non-slip boundary condition is used. In the computation, the mesh moves with the cavity rigidly. Based on the same third-order reconstruction, both directional-splitting flux and multidimensional flux will be tested in this case. The streamlines and the contour of pressure in the x–y plane at $z = 0$ and the streamlines in the x–z plane at $y = 0$ and $t = 2\pi$ and 4π are presented in Fig. 13 from the current multidimensional scheme. Complicated flow patterns appear. The U velocity profile at $t = 2\pi$, $t = 4\pi$, $t = 6\pi$ and $t = 12\pi$ in the x–y plane with $z = 0$ along the vertical centerline are presented in Fig. 11. The comparisons of the same velocity profile at $t = 2\pi$ and $t = 4\pi$ with the direct splitting solver are given in Fig. 12. Due to the absence of tangential derivatives in the flux evaluation in the directional splitting method, the directional splitting method has larger numerical dissipation than the multidimensional method.

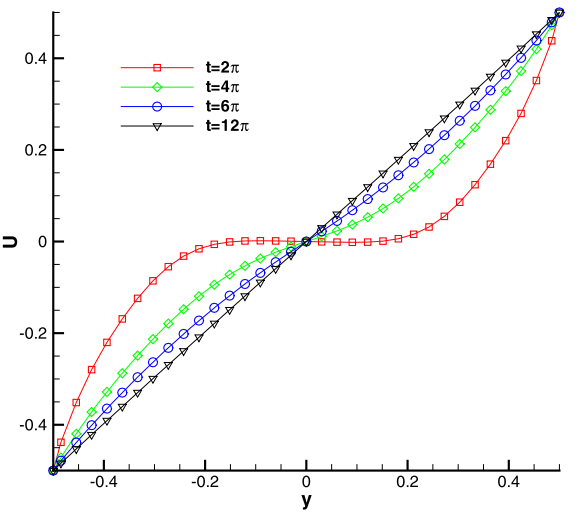

Fig. 11. U velocity profile from current scheme at $t = 2\pi$, $t = 4\pi$, $t = 6\pi$ and $t = 12\pi$ in the x–y plane at $z = 0$ along the vertical centerline.

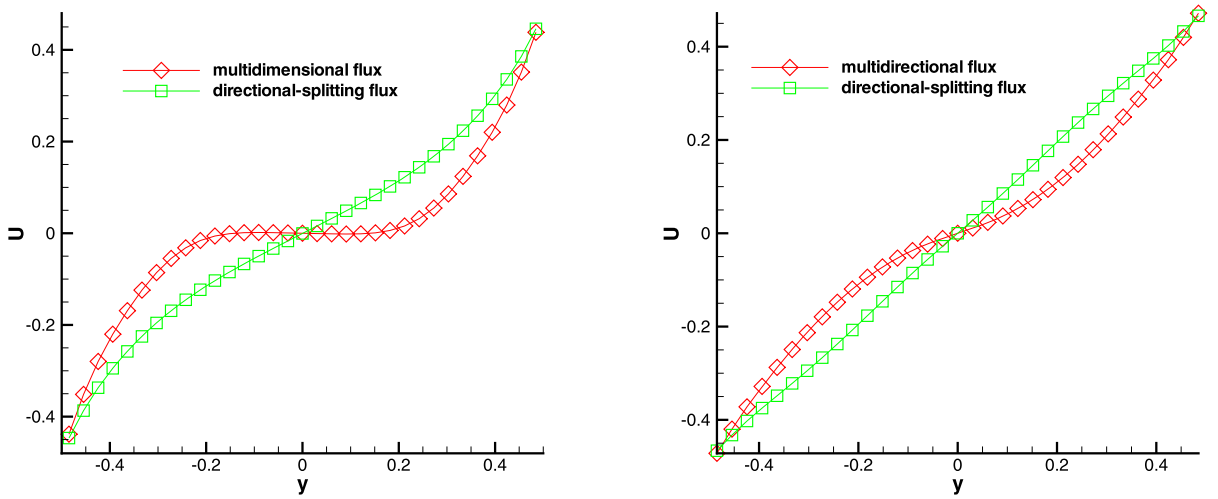

Fig. 12. U velocity profile at $t = 2\pi$ and $t = 4\pi$ along the vertical centerline in the x–y at $z = 0$. The squares are the profile from the directional-splitting method. The diamonds are the profile from the current multidimensional method.

4.7. Simple wave

In this case, the flow inside a tube driven by a piston is simulated [6]. Initially, the piston is located at $x = 0$ and the velocity of piston is 0. It starts to move with constant acceleration a when $t > 0$.

When the piston recedes from the gas with $a < 0$, a rarefaction wave originating from the piston will propagate into the undisturbed gas with a sound speed c_0. The flow motion will be confined in the region $x < c_0 t$. The exact solution of this problem is

$$u = -\frac{1}{\gamma}\left(c_0 - \frac{\gamma+1}{2}at\right) + \frac{1}{\gamma}\sqrt{\left(c_0 - \frac{\gamma+1}{2}at\right)^2 - 2a\gamma\left(x - c_0 t\right)}. \tag{27}$$

The analytical solutions of velocity u, sound speed c, pressure p, and density ρ are given by

$$c = c_0 + \frac{\gamma-1}{2}u,$$
$$p = p_0\left(1 + \frac{\gamma-1}{2}\frac{u}{c_0}\right)^{\frac{2\gamma}{\gamma-1}},$$
$$\rho = \rho_0\left(1 + \frac{\gamma-1}{2}\frac{u}{c_0}\right)^{\frac{2}{\gamma-1}}.$$

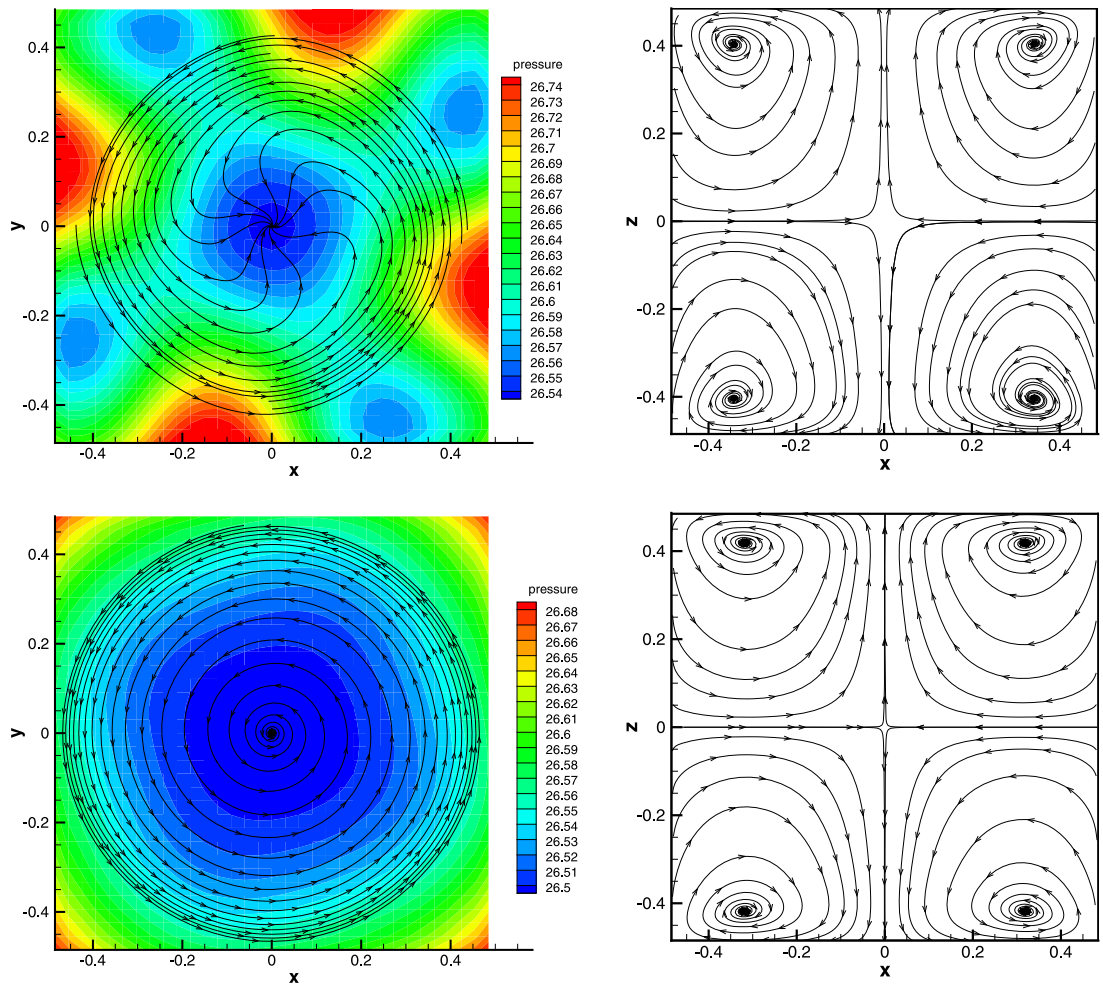

Fig. 13. The streamlines and the contours of pressure at the x–y plane at $z = 0$ (left) and the streamlines at the x–z plane at $y = 0$ (right) at $t = 2\pi$ and 4π for the 3D rotating cavity.

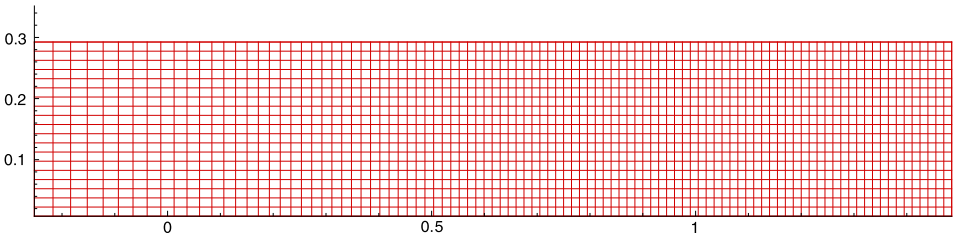

Fig. 14. The mesh of the rarefaction wave case at $t = 0.5$.

When a piston moves into the gas with $a > 0$, a compression wave originating from the piston will propagate into the undisturbed gas with the sound speed c_0 as well. Different from the rarefaction case, with the velocity of the piston increasing, the forward characteristics C^+ will converge and a discontinuity will be formed. Based on the analysis of characteristics, the discontinuity will appear at

$$t_* = \frac{2}{\gamma - 1}\frac{c_0}{a},$$

$$x_* = \frac{2}{\gamma - 1}\frac{c_0^2}{a}.$$

Before the appearance of the discontinuity, the analytical solutions for the rarefaction and compression waves are the same.

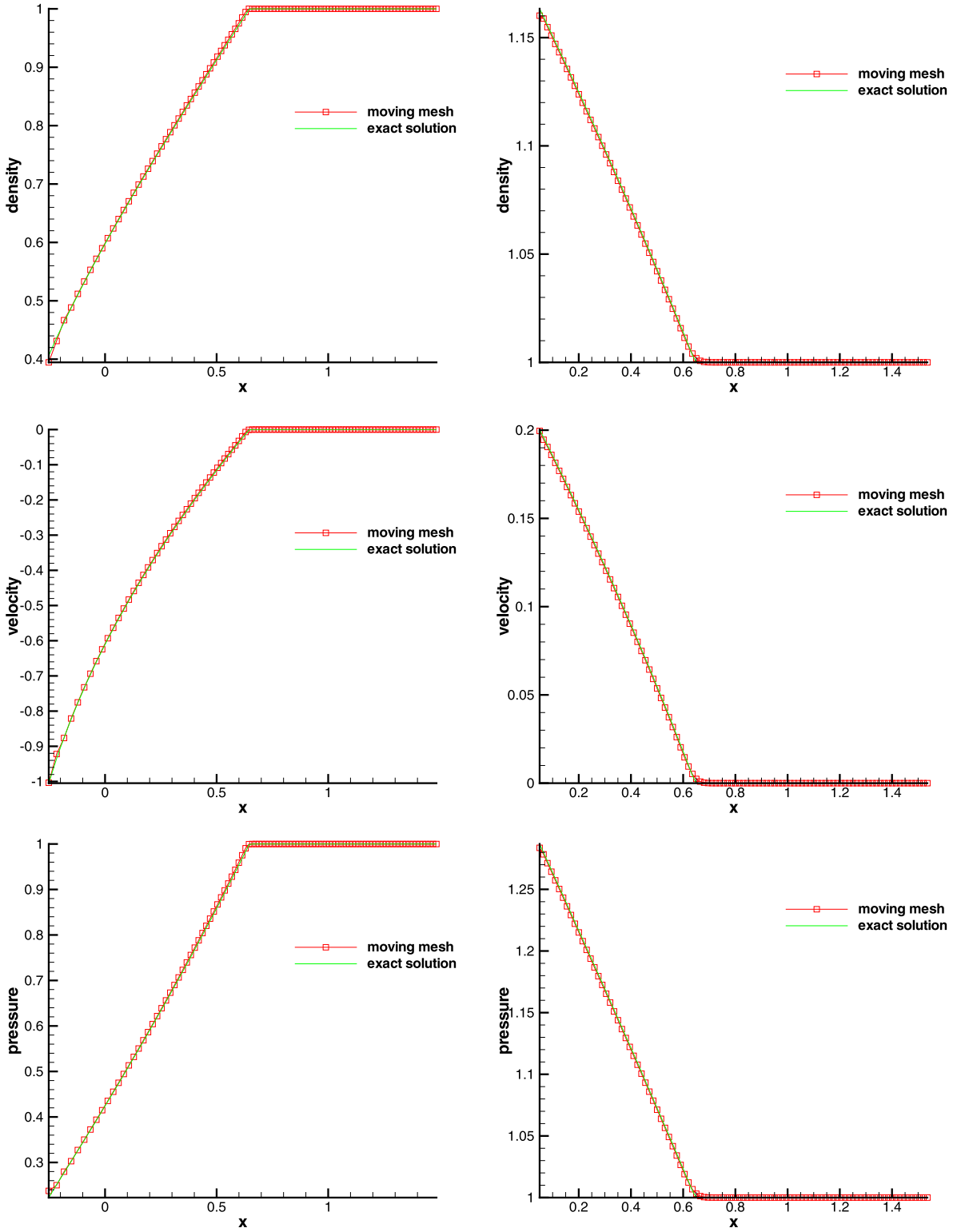

Fig. 15. The left contours are the numerical results and exact solution of the rarefaction wave at $t = 0.5$, and the right contours are the numerical results and exact solution of the compression wave. The solid lines are the exact solutions and the symbols represent the numerical results.

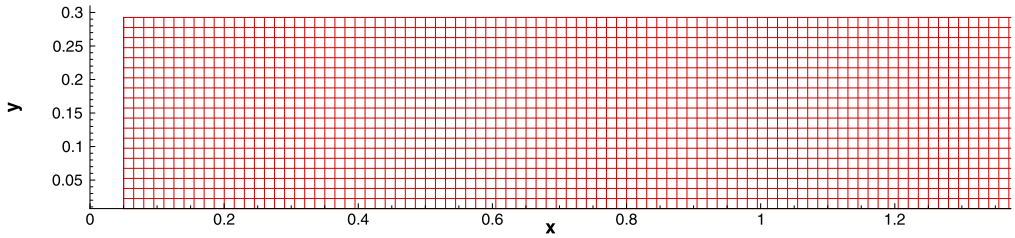

Fig. 16. The mesh of the compression wave case at $t = 0.5$.

In this case, the scheme with the inclusion of mesh acceleration is used in the computation. The initial condition is $(\rho_0, u_0, p_0) = (1, 0, 1)$, $\gamma = 5/3$, and a two-dimensional 100×20 mesh is adopted. In this case, the initial physical domain is $[0, 1.5] \times [0.0.3]$. On the left boundary, the reflecting boundary condition is used, and non-reflecting boundary conditions are used on other boundaries. For the rarefaction wave, the acceleration is $a = 2$. Based on the exact solution, the acceleration can be obtained by taking derivative of Eq. (27). The mesh moves according to the analytical solution of fluid velocity and acceleration and the mesh distribution at $t = 0.5$ is presented in Fig. 14. The density, velocity, and pressure, as well as the exact solutions, are presented in Fig. 15. The same case is tested by a scheme with mesh velocity without mesh acceleration [17]. The L^1 error of density in the current scheme can be reduced by 2.924% in comparison to the scheme without mesh acceleration. This is a significant amount of error reduction, and the techniques with mesh acceleration may be useful for aeroelastic applications.

For the compression case, the mesh moves with the velocity $U_g = at$ and an acceleration $a = 0.4$ uniformly, and the mesh is shown in Fig. 16 at $t = 0.5$. The density, velocity, pressure, and the exact solutions are presented in Fig. 15. In comparison with the solution without considering mesh acceleration, the current scheme can reduce the L^1 error of density by 2.5%.

5. Conclusion

In this paper, a generalized coordinate transformation with mesh velocity and acceleration is proposed. Under such a transformation, both mesh velocity and acceleration are used in the construction of the high-order moving-mesh gas-kinetic scheme, where the physical and geometrical variables are updated simultaneously. In the construction of the high-order scheme, the WENO method is used for the initial data reconstruction. With the initial piece-wise quadratic polynomials of macroscopic flow variables, a time-dependent gas distribution function is obtained at the moving and accelerating cell interface. In the current multidimensional scheme, both normal and tangential spatial derivatives are included explicitly in the gas evolution. The flux transports are obtained by taking moments of the time dependent gas distribution function, and integrating along a cell interface and over a whole time step. As a result, the current scheme can be efficient in comparison with the schemes equipped with Gaussian point integration and Runge–Kutta time stepping. The techniques with mesh acceleration may be useful for a delicate flow study, such as the aeroelastic interaction problem, where the mesh acceleration has not yet been taken into account [9].

This scheme is tested for both inviscid and viscous flow computations. The mesh velocity can be determined from different considerations, such as the mesh movement according to the flow velocity, the boundary velocity, or the mesh velocity determined by an elliptic solver. The numerical results are compared with the exact solutions and experimental measurements. Under the generalized coordinate transformation, a three-dimensional scheme has been developed as well.

Acknowledgements

This work was supported by Hong Kong Research Grant Council (621011, 620813) and HKUST (SBI14SC11, IRS15SC29). The authors would like to thank all reviewers for their constructive comments.

References

[1] S. Albensoeder, H.C. Kuhlmann, Accurate three-dimensional lid-driven cavity flow, J. Comput. Phys. 206 (2005) 536–558.
[2] D.J. Benson, Computational methods in Lagrangian and Eulerian hydrocodes, Comput. Methods Appl. Mech. Eng. 99 (1992) 235–394.
[3] P.L. Bhatnagar, E.P. Gross, M. Krook, A model for collision processes in gases I: small amplitude processes in charged and neutral one-component systems, Phys. Rev. 94 (1954) 511–525.
[4] C. Cercignani, The Boltzmann Equation and Its Applications, Springer-Verlag, 1988.
[5] S. Chapman, T.G. Cowling, The Mathematical Theory of Non-Uniform Gases, third edition, Cambridge University Press, 1990.
[6] R. Courant, K.O. Friedrichs, Supersonic Flow and Shock Waves, Springer-Verlag, New York/Berlin, 1948.
[7] G. De Vahl Davis, G.D. Mallinson, An evaluation of upwind and central difference approximations by a study of recirculating flow, Comput. Fluids 4 (1976) 29–43.
[8] J.K. Dukowicz, B.J.A. Meltz, Vorticity errors in multidimensional Lagrangian codes, J. Comput. Phys. 99 (1992) 115–134.
[9] M. Ghoreyshi, A. Jirásek, R.M. Cummings, Reduced order unsteady aerodynamic modeling for stability and control analysis using computational fluid dynamics, Prog. Aerosp. Sci. 71 (2014) 167–217.

[10] K. Goda, A multistep technique with implicit difference schemes for calculating two- or three-dimensional cavity flows, J. Comput. Phys. 30 (1979) 76–95.
[11] W.H. Hui, P.Y. Li, Z.W. Li, A unified coordinated system for solving the two-dimensional Euler equations, J. Comput. Phys. 153 (1999) 596–637.
[12] W.H. Hui, K. Xu, Computational Fluid Dynamics Based on the Unified Coordinates, Springer, 2012.
[13] W.H. Hui, The unified coordinate system in computational fluid dynamics, Commun. Comput. Phys. 2 (2007) 577–610.
[14] M. Ilgaz, I.H. Tuncer, A parallel gas-kinetic Bhatnagar–Gross–Krook method for the solution of viscous flows on two-dimensional hybrid grids, Int. J. Comput. Fluid Dyn. 23 (2009) 699–711.
[15] G.S. Jiang, C.W. Shu, Efficient implementation of weighted ENO schemes, J. Comput. Phys. 126 (1996) 202–228.
[16] J. Jiang, Y.H. Qian, Implicit gas-kinetic BGK scheme with multigrid for 3D stationary transonic high-Reynolds number flows, Comput. Fluids 66 (2012) 21–28.
[17] C. Jin, K. Xu, A unified moving grid gas-kinetic method in Eulerian space for viscous flow computation, J. Comput. Phys. 222 (2007) 155–175.
[18] C. Jin, K. Xu, S. Chen, A three dimensional gas-kinetic scheme with moving mesh for low-speed viscous flow computations, Adv. Appl. Math. Mech. 2 (2010) 746–762.
[19] G. Kumar, S.S. Girimaji, J. Kerimo, WENO-enhanced gas-kinetic scheme for direct simulations of compressible transition and turbulence, J. Comput. Phys. 234 (2013) 499–523.
[20] L.D. Landau, E.M. Lifshitz, Fluid Mechanics, second ed., Butterworth Heinemann, 1987.
[21] R.H. Landon, NACA 0012 oscillating and transient pitching, Data Set 3 in AGAR-R-702, Compendium of unsteady aerodynamic measurements, 1982.
[22] Q. Li, K. Xu, S. Fu, A high-order gas-kinetic Navier–Stokes flow solver, J. Comput. Phys. 229 (2010) 6715–6731.
[23] X.D. Liu, S. Osher, Weighted essentially non-oscillatory schemes, J. Comput. Phys. 115 (1994) 200–212.
[24] X.D. Liu, P.D. Lax, Solution of two-dimensional Riemann problems of gas dynamics by positive schemes, SIAM J. Sci. Comput. 19 (1998) 319–340.
[25] N. Liu, H.Z. Tang, A high-order accurate gas-kinetic scheme for one- and two-dimensional flow simulation, Commun. Comput. Phys. 15 (2014) 911–943.
[26] L. Mieussens, On the asymptotic preserving property of the unified gas-kinetic scheme for the diffusion limit of linear kinetic models, J. Comput. Phys. 253 (2013) 138–156.
[27] J. Luo, K. Xu, A high-order multidimensional gas-kinetic scheme for hydrodynamic equations, Sci. China, Technol. Sci. 56 (2013) 2370–2384.
[28] P.H. Maire, R. Abgrall, J. Breil, J. Ovadia, A cell-centered Lagrangian scheme for two-dimensional compressible flow problems, SIAM J. Sci. Comput. 224 (2007) 785–823.
[29] W. Shyy, H.S. Udaykumar, M.M. Rao, R.W. Smith, Computational Fluid Dynamics with Moving Boundaries, Taylor and Francis, Washington, DC, 1996.
[30] H.Z. Tang, A moving mesh method for the Euler flow calculations using a directional monitor function, Commun. Comput. Phys. 1 (2006) 656–676.
[31] H.Z. Tang, T. Tang, Adaptive mesh methods for one- and two-dimensional hyperbolic conservation laws, SIAM J. Numer. Anal. 41 (2003) 487–515.
[32] E. Toro, Riemann Solvers and Numerical Methods for Fluid Dynamics, Springer, 1997.
[33] P. Woodward, P. Colella, The numerical simulation of two dimensional fluids with strong shock, J. Comput. Phys. 54 (1984) 115–173.
[34] K. Xu, Gas Kinetic Schemes for Unsteady Compressible Flow Simulations, Lecture Note Ser., vol. 1998-03, Von Karman Institute for Fluid Dynamics, 1998.
[35] K. Xu, A well-balanced gas-kinetic scheme for the shallow-water equations with source terms, J. Comput. Phys. 178 (2002) 533–562.
[36] K. Xu, A gas-kinetic BGK scheme for the Navier–Stokes equations and its connection with artificial dissipation and Godunov method, J. Comput. Phys. 171 (2001) 289–335.
[37] K. Xu, J. Huang, A unified gas-kinetic scheme for continuum and rarefied flows, J. Comput. Phys. 229 (2010) 7747–7764.
[38] L.M. Yang, C. Shu, J. Wu, N. Zhao, Z.L. Lu, Circular function-based gas-kinetic scheme for simulation of inviscid compressible flows, J. Comput. Phys. 255 (2013) 540–557.